087

VIBRATION REDUCTION IN ROTORCRAFT USING ACTIVE MICROFLAPS

Ashwani K. Padthe, Ph.D. Candidate, akpadthe@umich.edu

Li Liu, Postdoctoral Researcher, ryanliu@umich.edu

Peretz P. Friedmann, François-Xavier Bagnoud Professor of Aerospace Engineering, peretzf@umich.edu

Department of Aerospace Engineering
University of Michigan, Ann Arbor, MI, United States

Abstract

Active Gurney flaps, or microflaps, are studied to determine their effectiveness in reducing vibrations in rotorcraft. A CFD based reduced order aerodynamic model (ROM) capable of modeling the unsteady effects of a microflap was incorporated into a comprehensive rotorcraft simulation code AVINOR. The ROM is constructed based on the Rational Function Approximation (RFA) approach, which results in a state-space time domain aerodynamic model suitable for use with comprehensive codes. Vibration reduction studies were conducted on a hingeless rotor configuration resembling MBB BO-105, using the relaxed Higher Harmonic Control (HHC) algorithm. Various spanwise configurations of the microflap, including a single, a dual, and a segmented five-microflap configuration, were considered and compared to conventional trailing edge flaps. The results indicate that the microflap is an effective device for vibration reduction in rotorcraft, capable of achieving substantial reductions in excess of 80%. However, the 1.5%c microflap was found to incur 3.6% performance penalty due to the increased drag. Parametric studies on microflap sizing suggest that a microflap configuration with the height of less than 1%c may be best in achieving substantial vibration reduction while mitigating performance penalty. Finally, the microflap was also found to be effective over a wide range of flight conditions.

Presented at the 36th European Rotorcraft Forum, Paris, France, September 7-9, 2010.

Nomenclature

b	Rotor blade semi-chord $= c_b/2$
c_b	Rotor blade chord
$\mathbf{C}_0, \mathbf{C}_1, ..., \mathbf{C}_{n+1}$	Rational function coefficient matrices
C_d	Drag coefficient
C_{df}	Fuselage drag coefficient
C_{hm}	Hinge moment coefficient
C_l	Lift coefficient
C_m	Moment coefficient
C_W	Helicopter weight coefficient
$\mathbf{D}, \mathbf{E}, \mathbf{R}$	Matrices defined in the RFA model
e	Blade root offset
f	Equivalent flat plate area of fuselage
$\mathbf{f}$	Generalized load column matrix
$\mathbf{G}$	Laplace transform of $\mathbf{f}(\bar{t})U(\bar{t})$
$\mathbf{h}$	Generalized motion column matrix
$\mathbf{H}$	Laplace transform of $\mathbf{h}(\bar{t})$
k	Reduced frequency $= 2\pi\nu b/U$
L_b	Blade length
M	Mach number
M_b	Blade mass
N_b	Number of rotor blades
n_L	Number of lag terms
P_R	Average rotor power
$\mathbf{Q}$	Aerodynamic transfer function matrix
$\tilde{\mathbf{Q}}$	Approximation of $\mathbf{Q}$
R	Rotor blade radius
s	Laplace variable
$\bar{s}$	Nondim. Laplace variable $= sb/U$

$\mathbf{T}$	Sensitivity matrix relating control input to the plant output
t	Time
$\bar{t}$	Reduced time $= \frac{1}{b}\int_0^t U(\tau)d\tau$
$U(t)$	Freestream velocity, time-dependent
$\mathbf{u}$	control input vector
W_0, W_1	Generalized airfoil motions
X_A	Offset between the aerodynamic center and the elastic axis
X_{Ib}	Offset of the blade cross-sectional center of mass from the elastic axis
X_{FA}, Z_{FA}	Longitudinal and vertical offsets between rotor hub and helicopter aerodynamic center
X_{FC}, Z_{FC}	Longitudinal and vertical offsets between rotor hub and helicopter center of gravity
$\mathbf{x}(t)$	Aerodynamic state vector
$\mathbf{z}$	Plant output vector
α	Airfoil angle of attack
α_R	Rotor shaft angle
γ	Lock number
γ_n	Rational approximant poles
δ_f	Flap deflection
δ_{Nc}, δ_{Ns}	N/rev cosine and sine amplitudes of δ_f
ϕ_R	Lateral roll angle
μ	Advance ratio
θ_0	Collective pitch
θ_{0t}	Tail rotor pitch angle
θ_{1c}, θ_{1s}	cyclic pitch components
θ_{FP}	Flight path angle
θ_{tw}	Blade pretwist distribution
σ	Rotor solidity
$\omega_F, \omega_L, \omega_T$	Blade flap, lag and torsional natural frequencies
Ω	Rotor angular speed
ψ	Azimuth angle

Introduction and Background

The Gurney flap is a small tab typically less than 5%c in height and is attached normal to the airfoil surface at the trailing edge as shown in Fig. 1. Originally used by Dan Gurney on race cars to increase the downward force generated by the spoiler, the Gurney flap has been shown to be capable of increasing the maximum lift coefficient of an airfoil by as much as 60%. One of the earliest experimental studies on aerodynamics of a Gurney flap was conducted by Liebeck [1] who found that the Gurney flap caused the flow to turn around the trailing edge resulting in the formation of two counter-rotating vortices behind the flap as shown in Fig. 1. The turning of the flow shifts the trailing edge stagnation point to the bottom edge of the microflap thus changing the Kutta condition and increasing the effective camber of the airfoil. Subsequently these experimental observations have been confirmed using CFD computations and flow visualization techniques [2–7]. These studies have shown that despite the small size the Gurney flap is an effective lift enhancement device.

Active Gurney flaps that are deployable as opposed to being permanently fixed are referred to as microflaps in this study. This device has the potential for high bandwidth control with low actuation power requirements, minimal loss in structural stiffness of the wing, and lower wing warping when compared to the conventional control surfaces. Microflaps have been studied for various applications such as control of high aspect ratio flexible aircraft [8, 9], wing trailing edge vortex alleviation [10–12], aerodynamic load control for wind turbine blades [6, 13, 14], and for rotorcraft performance enhancement [15–17]. It was found that the deployable microflaps can increase flutter speed of a highly flexible wing by up to 22% [8]. Recent studies for fixed wing applications [10–12] suggest that microflaps can also be used for wake alleviation by inducing time-varying perturbations that excite vortex instability in the wake. The potential of microflaps with application to active load control in wind turbine blades was explored computationally and experimentally on representative turbine airfoil sections [6, 13]. Substantial reduction in turbine blade root bending moment (reduction of peak bending moment ranging from 30-50%) was observed in Ref. [14] using the microflap approach. In [14] the microflap effect was simulated based on static Gurney flap measurements. Preliminary studies on rotorcraft performance enhancement using permanently attached Gurney flaps (of size less than 2%c) have been conducted in Ref. [15]. The effect of Gurney flaps on the airfoil lift and drag was modeled as a curve fit of experimental results obtained for flaps of various sizes. Wind-tunnel tests conducted on a model helicopter confirmed that Gurney flaps may have beneficial ef-

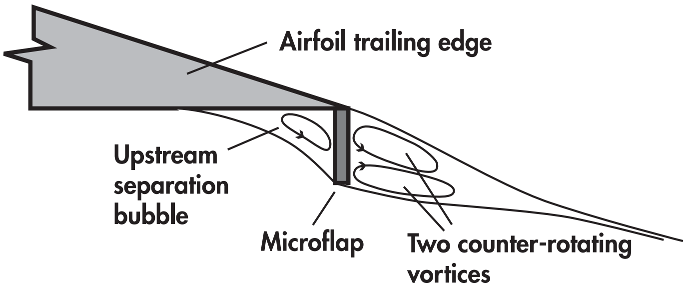

Figure 1. An illustration of the Gurney flap.

fects on rotorcraft performance. More recently, deployable microflaps have been studied with active control strategies to enhance rotorcraft performance [16–18]. A relatively simple deployment schedule where the microflaps are deployed primarily on retreating side of the disk was used, and the maximum thrust of the rotor was enhanced by 10% using microflaps with a height of 1%c distributed along the entire blade span.

During the last fifteen years, various active control approaches, including conventional trailing edge flaps, have been found to be effective for vibration reduction in rotorcraft [19–24]. The size advantage of the microflap when compared to the plain flaps will allow high bandwidth actuation with small actuation power, and it is a potentially attractive candidate for active control of helicopter vibration. In a recent study [25] preliminary results were presented to demonstrate the potential of the microflap for vibration reduction in rotorcraft. A 1.5%c microflap was actuated in open loop mode with control harmonics of 2-5/rev, on a rotor configuration resembling an MBB BO-105 hingeless rotor. Various microflap configurations, shown in Fig. 2, were also compared in Ref. [25]. The aerodynamic effect of the microflap was modeled using a nonlinear reduced order model (ROM) constructed from CFD data [26]. It was found that the microflap is effective in reducing vibratory hub loads; in particular, maximum vibration reduction of 52% in the dominant vertical shear component was obtained using 4/rev open loop input. The microflap spanwise configuration employed in Ref. [25] was identical to that used in earlier studies for conventional active flaps with chord size of 20-25%c.

The overall objective of this paper is to explore the potential of the microflap for vibration reduction in rotorcraft, using a comprehensive rotorcraft simulation code combined with the CFD-based microflap reduced order model [26]. Careful parametric studies of microflap sizing and location are conducted so as to determine the optimal configuration

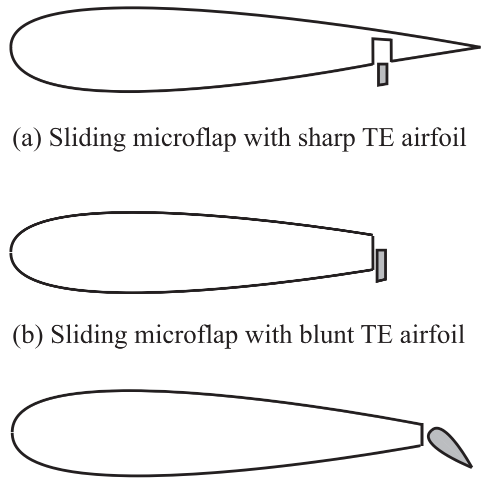

(a) Sliding microflap with sharp TE airfoil

(b) Sliding microflap with blunt TE airfoil

(c) Rotating microflap resembling plain flap

Figure 2. Various microflap configurations.

for vibration reduction. The specific objectives of the proposed paper are:

1. Incorporate a refined reduced-order aerodynamic model developed in [26] into the comprehensive rotorcraft simulation code AVINOR [27];

2. Study and compare the effect of various microflap configurations for vibration reduction on a representative rotor configuration;

3. Compare the effectiveness of the microflap for vibration reduction to similar plain flap configurations;

4. Provide a comprehensive assessment of the potential of the microflap device for active vibration reduction in rotorcraft, including performance penalty considerations.

A Combined CFD and Rational Function Approximation Based ROM for Control Surfaces

The strong nonlinear nature of viscous flow behind the microflap implies that the effect of the microflap needs to be considered using a CFD based approach. As mentioned earlier, various CFD tools have been used to determine the aerodynamic characteristics of a Gurney flap or microflap with reasonable accuracy. However, the computational costs of coupling CFD solvers directly with rotorcraft simulation codes are prohibitive when conducting parametric trend studies involving active control. A nonlinear CFD based reduced-order aerodynamic model developed in [26] has been shown to be accurate, efficient, and suitable for combination with comprehensive rotorcraft codes. Furthermore, this model can be used to represent the effects of various trailing edge control devices, including microflaps and conventional flaps. To develop the reduced-order model, a compressible unsteady Reynolds-Averaged Navier-Stokes CFD solver is used to generate frequency domain aerodynamic response, which is then converted to the time-domain using the Rational Function Approximation (RFA) approach.

The RFA approach has been used in the past to generate a Laplace transform or state variable representation of the unsteady aerodynamic loading on a wing section for fixed wing applications [28–31] as well as rotary wing applications [32]. The resulting reduced-order aerodynamic model is a state-space, time domain model that accounts for flow unsteadiness and compressibility. In Ref. 32 the RFA aerodynamic model was developed for modeling the aerodynamic response of a two-dimensional airfoil/trailing edge flap combination. Recently, the accuracy of this model was also verified by comparing its unsteady aerodynamic load predictions with CFD for a two-dimensional airfoil/oscillating flap combination over a wide range of aerodynamic conditions representative of rotorcraft applications [33, 34].

The new CFD based reduced order model developed using the RFA approach, referred to as the CFD+RFA model, has the same advantages as the original RFA model: 1) it allows a convenient combination of the aerodynamics with the structural dynamic model; 2) it is suitable for the solution of the combined system which is governed by equations with periodic coefficients, since it facilitates the use of direct numerical integration; and 3) it provides a degree of computational efficiency required by the implementation of active control techniques such as trailing edge flaps and microflaps. Therefore, the CFD+RFA model is ideally suited for use with comprehensive codes for aeroelastic simulations and active control studies.

Concise description of the RFA approach

The RFA approach used in conjunction with CFD to obtain the ROM is concisely described below. Additional details can be found in Ref. [26]. The RFA model is based on Roger's approximation [28]

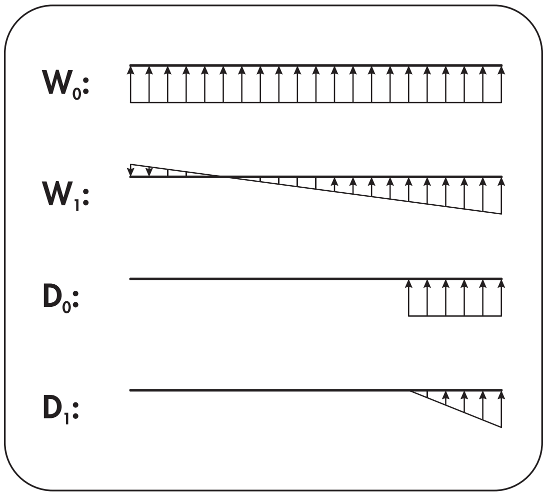

Figure 3. Normal velocity distribution corresponding to generalized airfoil and plain flap motions.

and represents a relation between generalized aerodynamic loads and generalized motions of the aerodynamic surface in Laplace domain as

$$\mathbf{G}(\bar{s}) = \mathbf{Q}(\bar{s})\mathbf{H}(\bar{s}), \tag{1}$$

where $\mathbf{G}(\bar{s})$ and $\mathbf{H}(\bar{s})$ are the Laplace transforms of the column matrices representing generalized aerodynamic load and generalized motion, respectively. The aerodynamic transfer matrix $\mathbf{Q}(\bar{s})$ is approximated using the Least Squares approach with a rational expression of the form

$$\tilde{\mathbf{Q}}(\bar{s}) = \mathbf{C}_0 + \mathbf{C}_1\bar{s} + \sum_{n=1}^{n_L} \frac{\bar{s}}{\bar{s} + \gamma_n}\mathbf{C}_{n+1}. \tag{2}$$

Equation (2) is usually denoted as Roger's approximation. The poles $\gamma_1, \gamma_2, ..., \gamma_{n_L}$ are assumed to be positive valued to produce stable open loop roots, but are non-critical to the approximation. Arbitrary motions of the airfoil and a conventional trailing edge flap are represented by four generalized motions shown in Fig. 3. The normal velocity distributions shown in Fig. 3 correspond to two generalized airfoil motions (denoted by W_0 and W_1) and two generalized flap motions (denoted by D_0 and D_1). The two generalized flap motions shown in Fig. 3 represent the angular deflection of a conventional trailing edge flap. For the microflap, the concept of normal velocity distributions is no longer meaningful; therefore, the microflap motion is simply characterized by the deflection δ_f and the effect of flap deflection rate is assumed to be negligible. This assumption was made since the aerodynamic response of the airfoil to the flap deflection rate obtained from CFD simulations was found to be insignificant.

In order to find $\tilde{\mathbf{Q}}(\bar{s})$, tabulated oscillatory airloads, i.e. sectional lift, moment and hinge moment, need to be obtained corresponding to the generalized motions. In the original RFA implementation, the oscillatory airloads in the frequency domain were obtained from a potential flow solver which provides a two-dimensional doublet lattice (DL) solution of Possio's integral equation [32]. This approach was found to be very efficient for generating a set of aerodynamic response data for the generalized motions of airfoil/flap combination. The frequency domain information is generated for an appropriate set of reduced frequencies and Mach numbers, encompassing the entire range of unsteady flow conditions encountered in practical applications.

To construct a CFD based RFA model, a commercially available CFD solver CFD++ [35, 36] developed by METACOMP Technologies was used to generate the frequency domain responses. This results in a ROM that captures the strong viscous flow behind a microflap, and also provides unsteady drag predictions which cannot be obtained from potential flow theory. Furthermore, significant flow nonlinearities associated with viscous effects or shock wave formation are also accounted for in this approach.

A state space representation of the RFA aerodynamic model is derived by defining a generalized motion vector $\mathbf{h}$ and a generalized load vector $\mathbf{f}$, as:

$$\mathbf{h} = \left\{ \begin{array}{c} W_0 \\ W_1 \\ D_0 \\ D_1 \end{array} \right\} \quad \text{for plain flap, or} \tag{3}$$

$$\mathbf{h} = \left\{ \begin{array}{c} W_0 \\ W_1 \\ \delta_f \end{array} \right\} \quad \text{for microflap,} \tag{4}$$

and

$$\mathbf{f} = \left\{ \begin{array}{c} \mathrm{C}_l \\ \mathrm{C}_m \\ \mathrm{C}_d \\ \mathrm{C}_{hm} \end{array} \right\} \tag{5}$$

Note that hinge moment C_{hm} is applicable only for conventional flaps and is not needed for microflaps. The rational approximant $\tilde{\mathbf{Q}}$ in Eq. (2) can be transformed to the time domain using the inverse Laplace transform, which yields the final form of the state space model, given below

$$\begin{aligned} \dot{\mathbf{x}}(t) &= \frac{U(t)}{b}\mathbf{R}(M,\alpha,\delta_f)\mathbf{x}(t) + \mathbf{E}(M,\alpha,\delta_f)\dot{\mathbf{h}}(t), \\ \mathbf{f}(t) &= \frac{1}{U(t)}\Big[\mathbf{C}_0(M,\alpha,\delta_f)\mathbf{h}(t) \\ &\quad + \mathbf{C}_1(M,\alpha,\delta_f)\frac{b}{U(t)}\dot{\mathbf{h}}(t) + \mathbf{D}\mathbf{x}(t)\Big]. \end{aligned} \tag{6}$$

where the definitions of matrices $\mathbf{D}$, $\mathbf{R}$ and $\mathbf{E}$ can be found in Ref. [32].

Note that in order to account for flow nonlinearities encountered at high Mach numbers, large angles of attack and flap deflections, the RFA model has been enhanced by using a technique referred to as *model scheduling* [37], wherein different sets of RFA coefficients are generated at appropriate combinations of the Mach number, angle of attack, and flap deflection angle. Specifically, the RFA model is modified by allowing the coefficient matrices, i.e., $\mathbf{R}, \mathbf{E}, \mathbf{C}_0, \mathbf{C}_1$,..., to vary with M, α, and δ_f, as indicated in Eq. (6).

CFD simulations

As stated earlier, the CFD results for constructing the ROM are obtained using the CFD++ code, which is capable of solving the compressible unsteady Reynolds-Averaged Navier-Stokes equations. It uses a unified grid methodology that can handle a variety of structured, unstructured, multi-block meshes and cell types, including patched and overset grid features. Spatial discretization is based on a second order multi-dimensional Total Variation Diminishing (TVD) scheme. For temporal scheme an implicit algorithm with dual time-stepping is employed to perform time-dependent flow simulations, with multigrid convergence acceleration. Various turbulence models are available in CFD++ and the Spalart-Allmaras model is used for the current study, assuming fully turbulent boundary layer.

In Ref. [26] three candidate microflap configurations were examined and compared for their effectiveness in generating unsteady airloads. The sharp trailing edge configuration (Fig. 2a) was determined to be the best compromise between the aerodynamic benefits and the ease of implementation in rotor blades; therefore it is chosen for the current study. The CFD grids employed for this configuration are shown in Fig. 4(b); grids for a 20% plain

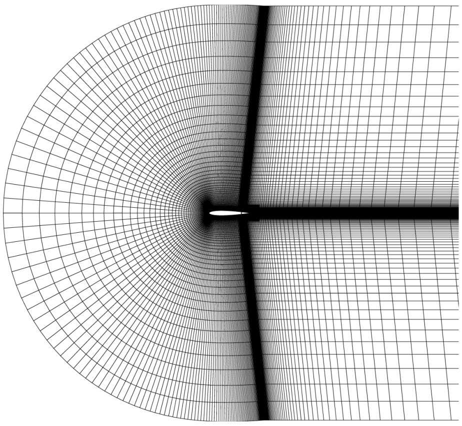

(a) Grid overview

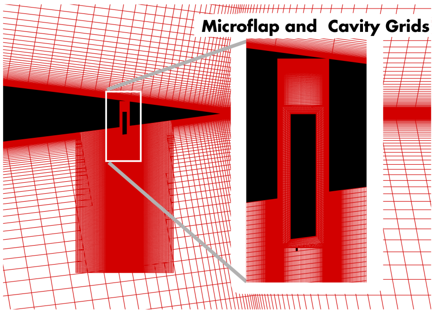

(b) Close-up grid for microflap

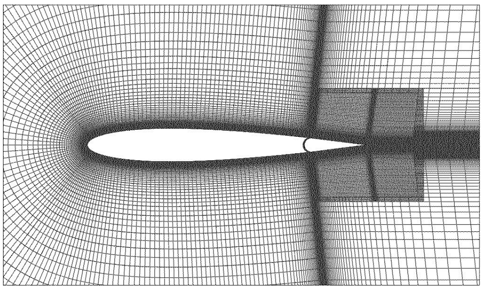

(c) Close-up grid for plain flap

Figure 4. Grids used for CFD simulations.

flap are also shown in Fig. 4(c). The overall computational domain is shown in Fig. 4(a) which contains approximately 90,000 grid points. The CFD grids for the various microflap or plain flap configurations are generated using the overset approach, which is a convenient method for modeling complex geometries and moving components with large relative motions. The grids are clustered at the airfoil wall boundaries such that the dimensionless distance y^+ of the first grid point off the wall is less than 1 and the equations are solved directly to the walls without assuming wall functions.

In order to generate a ROM that can represent the entire range of flow conditions encountered by the blades at various advance ratios, CFD simulations are conducted for Mach numbers ranging from 0.05 to 0.9 and angles of attack ranging from 0° to 15°. All the simulations were carried out for the NACA0012 airfoil at Reynolds number 2.1×10^6. At each flow condition defined by the free stream Mach number and the airfoil mean angle of attack, simulations are performed to generate frequency domain data corresponding to the generalized motions at reduced frequency values ranging from 0.02 to 0.2 with an increment of 0.02. Note that the 5/rev frequency at 0.75R span location on the rotor blade of a representative MBB BO-105 rotor configuration corresponds to a reduced frequency of 0.18. The frequency domain data obtained through CFD simulations is subsequently used to generate the coefficients C_0, C_1, ... , C_n in the CFD+RFA reduced order model. These coefficients are generated from CFD results at simulated flow conditions and then a "shape-preserving" piecewise cubic Hermite polynomial interpolation scheme [38–40] is used to evaluate the coefficients at intermediate flow conditions. In this interpolation scheme, the slopes of the interpolating function at the data points are determined such that the function evaluations do not significantly overshoot the fitting data values. Complete validations of the CFD+RFA model by comparing the ROM predictions to direct CFD simulations can be found in Refs. [26] and [41], for a wide range of flow conditions and unsteady microflap/plain flap deflections.

Description of the Aeroelastic Analysis Code

Active vibration reduction studies with the microflap are conducted using a comprehensive rotorcraft aeroelastic analysis code AVINOR (Active Vibration and Noise Reduction) which has been extensively validated [22, 27, 42]. The CFD+RFA model as described earlier has been incorporated into AVINOR and is used to model the effect of microflaps, as well as plain trailing edge flaps for comparison purposes. The ability to model segmented multiple microflap configurations has been incorporated into the code. The principal ingredients of the AVINOR code are concisely summarized in the following subsections.

Aerodynamic model

The blade/flap sectional aerodynamic loads for attached flow are calculated using the CFD+RFA model, that was described earlier. This model provides unsteady lift, moment, as well as drag predictions for both plain flap and microflap configurations. The RFA model for the blade-flap combination is linked to a free wake model described in [22,42], which produces a spanwise and azimuthally varying inflow distribution. For separated flow regime, the aerodynamic loads are calculated by the ONERA dynamic stall model.

Structural dynamic model

The structural dynamic model used for the present study consists of a four-bladed hingeless rotor, with fully coupled flap-lag-torsional dynamics with moderate deflections. The structural equations of motion are discretized using the global Galerkin method, based upon the free vibration modes of the rotating blade. The dynamics of the blade are represented by three flap, two lead-lag, and two torsional modes. Each free vibration mode was calculated using the first nine exact non-rotating modes of a uniform cantilevered beam. The effect of control surfaces such as the trailing-edge plain flap or the microflap on the structural properties of the blade is assumed to be negligible. The control surfaces influence the behavior of the blade only through their effect on the aerodynamic and inertial loads.

Coupled aeroelastic response/trim solution

The combined structural and aerodynamic equations form a system of coupled differential equations that can be cast in state-variable form. The trim procedure used is based on a propulsive trim with three force equations (longitudinal, lateral, and vertical) and three moment equations (roll, pitch, and yaw) corresponding to a helicopter in free flight. A simplified tail rotor model, based on uniform inflow and blade element theory, is used. The six trim variables are the rotor shaft angle α_R, the collective pitch θ_0, the cyclic pitch θ_{1s} and θ_{1c}, the tail rotor constant pitch θ_{0t}, and lateral roll angle ϕ_R. The coupled trim/aeroelastic equations are solved in time using the ODE solver DDEABM, which is a predictor-corrector based Adams-Bashforth differential system solver.

Control Algorithm for Vibration Reduction

The Higher Harmonic Control (HHC) algorithm has been used in the past to successfully achieve vibration and noise reduction in rotorcraft [22]. A detailed description of the algorithm, including robustness and stability analyses, can be found in [43]. The HHC algorithm is based on a linear, quasi-static, frequency-domain model of the helicopter response. For a 4-bladed rotor, the control input $\mathbf{u}$ is a combination of the 2/rev, 3/rev, 4/rev, and 5/rev harmonic components of the flap deflection. Note that the flap deflection referred to here in this section applies to both the microflap and the conventional trailing-edge flap. The total flap deflection is thus given by

$$\delta_f(\psi) = \sum_{N=2}^{5} [\delta_{Nc}\cos(N\psi) + \delta_{Ns}\sin(N\psi)]. \tag{7}$$

The output $\mathbf{z}$ is a combination of the 4/rev vibratory hub loads and moments. The control input $\mathbf{u}$ is related to the vibration levels through a transfer matrix $\mathbf{T}$ given by

$$\mathbf{T} = \frac{\partial \mathbf{z}}{\partial \mathbf{u}}. \tag{8}$$

The control strategy is based on the minimization of a performance index that is a quadratic function of the vibration magnitudes $\mathbf{z}$ and the control amplitudes $\mathbf{u}$:

$$J(\mathbf{z}_i, \mathbf{u}_i) = \mathbf{z}_i^T \mathbf{W}_z \mathbf{z}_i + \mathbf{u}_i^T \mathbf{W}_u \mathbf{u}_i, \tag{9}$$

where the $\mathbf{W}_z$ and $\mathbf{W}_u$ are the weighted matrices on the vibration magnitudes and control input, respectively. The subscript i refers to the i^{th} control step, reflecting the discrete-time nature of the controller. The optimal control is determined by solving the condition for minimization of the cost function J:

$$\frac{\partial J(\mathbf{z}_i, \mathbf{u}_i)}{\partial \mathbf{u}_i} = 0, \tag{10}$$

which yields the optimal control

$$\mathbf{u}_i = -\mathbf{D}^{-1}\mathbf{T}^T\mathbf{W}_z\{\mathbf{z}_{i-1} - \mathbf{T}\mathbf{u}_{i-1}\}, \tag{11}$$

where

$$\mathbf{D} = \mathbf{T}^T\mathbf{W}_z\mathbf{T} + \mathbf{W}_u. \tag{12}$$

For a perfectly linear system, the algorithm converges to the optimal value in a single step. However, if the helicopter response cannot be represented by a linear system, the algorithm might take multiple steps to converge to the optimal value. Several variants of the HHC algorithm, including a relaxed and an adaptive version, have been shown to improve the robustness of the algorithm to model uncertainties [43]. In the present study, the relaxed HHC algorithm is used for examining vibration reduction with the microflap and the 20%c plain flap. To impose saturation limits on the flap deflection, an algorithm developed in [44] is used. In this approach, the control weighting matrix is adjusted iteratively until the flap deflection is properly constrained.

Results and Discussions

In this section, results for vibration reduction with various microflap configuration are presented for a heavy blade-vortex interaction flight condition, on a representative rotor configuration resembling MBB BO-105 hingeless rotor. The effectiveness of the microflap is also compared to similar plain flap configurations. Subsequently, results from parametric studies of the microflap on flap chord sizing and at various forward flight conditions are discussed.

Rotor/flap configurations

The rotor parameters used in this study resemble those of a four-bladed MBB BO-105 hingeless rotor and are listed in Table 1.

Table 1. Rotor parameters used for vibration reduction studies.

Dimensional Rotor Data	
$R = 4.91$ m	
$M_b = 27.35$ kg	
$\Omega = 425$ RPM	
Nondimensional Rotor Data	
$N_b = 4$	$L_b = 1.0$
$c_b = 0.05498$	$\theta_{\text{tw}} = -8°$
$e = 0$	
$X_A = 0$	$X_{Ib} = 0$
$\omega_F = 1.124, 3.40, 7.60$	$\omega_L = 0.732, 4.458$
$\omega_T = 3.17, 9.08$	
$\gamma = 5.5$	$\sigma = 0.07$
Helicopter Data	
$C_W = 0.005$	$fC_{df} = 0.031$
$X_{FA} = 0.0$	$Z_{FA} = 0.25$
$X_{FC} = 0.0$	$Z_{FC} = 0.5$

The sharp trailing edge configuration, shown in Fig. 5, was chosen as the microflap configuration. The microflap, 1.5%c in height, slides in and out of a cavity, located at 6%c from the sharp trailing edge of the airfoil.

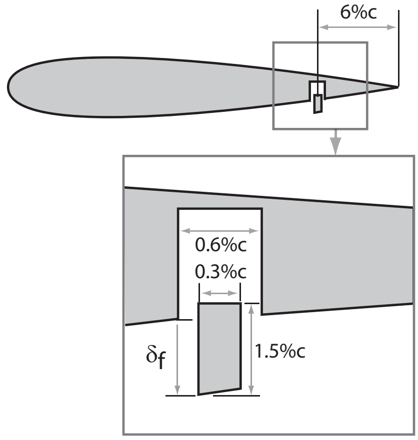

Figure 5. Oscillating microflap in a cavity for the sharp trailing-edge configuration.

Three different spanwise configurations of the microflaps on the rotor blade are considered in this study. The first configuration, shown in Figure 6(a), has a single microflap with 0.12R spanwise length centered at 0.75R. The second configuration, shown in Figure 6(b), has two microflaps each with 0.06R spanwise length centered at 0.72R and 0.92R, respectively. The third configuration shown in Figure 6(c), has five microflaps each 0.05R in spanwise length placed adjacently. For comparison purposes, vibration reduction studies with the single and dual plain flap configurations with 0.20%c flap chord were

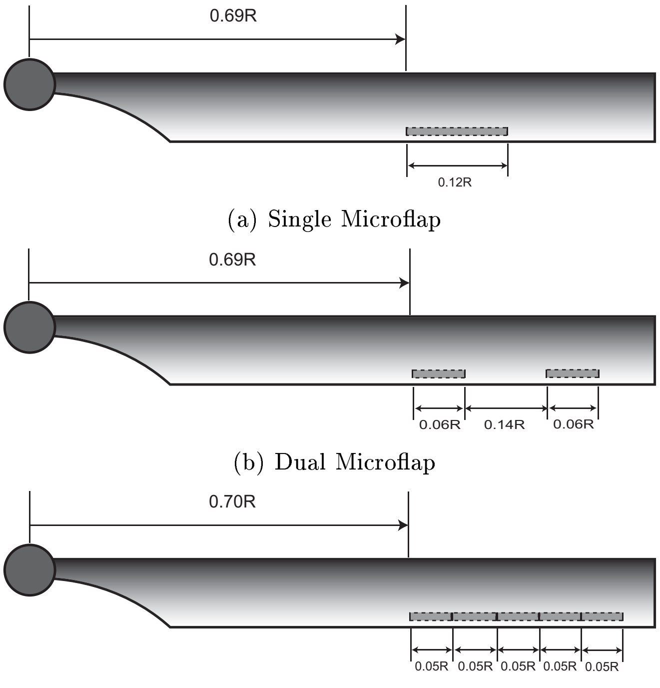

(a) Single Microflap

(b) Dual Microflap

(c) 5 Microflaps

Figure 6. Various spanwise configurations of the microflap on the rotor blade

also conducted for identical spanwise flap configurations.

Vibratory loads predictions using CFD based ROM

In order to examine the results from the CFD based ROM, the 4/rev baseline vibratory hub loads and moments obtained using the CFD+RFA aerodynamic model are compared with those obtained using the earlier potential flow based RFA model, at a flight condition where the advance ratio $\mu = 0.15$ and weight coefficient $C_W = 0.005$. The comparisons are shown in Figure 7, with the potential flow based results indicated by "DL+RFA". It is important to note that the DL+RFA model cannot predict the unsteady drag due to both airfoil and flap oscillations. Further, it does not account for the nonlinearities in the unsteady aerodynamic loads at higher angles of attack or Mach numbers. As shown in Fig. 7, the CFD+RFA model predicts 94% higher longitudinal, 150% higher lateral, and 43% higher vertical shear forces compared to the DL+RFA model. The CFD+RFA model also predicts a higher yawing moment as compared to the DL+RFA model. A primary source of difference in the inplane (longitudinal and lateral) vibratory loads and the yawing moment is attributed to the

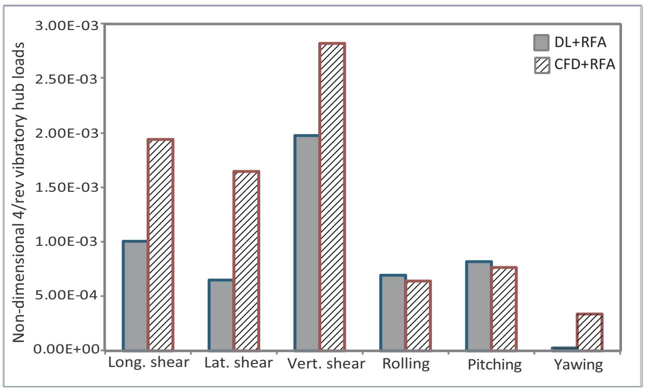

Figure 7. Comparison of baseline 4/rev vibratory hub loads and moments predictions from the CFD+RFA model with DL+RFA model; $\mu = 0.15$.

modeling of unsteady drag in CFD+RFA model. By contrast, the difference observed in vertical shear is primarily due to discrepancies in unsteady lift and moment predictions by the CFD based and the DL+RFA models [34, 41].

Vibration reduction with microflap

Vibration reduction with the three microflap configurations described earlier is conducted for an advance ratio $\mu = 0.15$ and weight coefficient $C_W = 0.005$. The rotor is trimmed for level steady flight. After trimming the rotor, the HHC controller is engaged to study the effectiveness of the microflaps in reducing the 4/rev vibratory hub loads, with the control input consisting of a combination of the 2/rev, 3/rev, 4/rev, and 5/rev harmonic components of the microflap deflection. After the optimal microflap deflection is found by the HHC controller, the rotor is re-trimmed to ensure that the rotor operates under the same trim conditions.

Vibratory hub loads obtained using the various spanwise configurations of the microflap, illustrated in Figures 6(a)-6(c), are shown in Figure 8. All three configurations considered here produce a substantial amount of vibration reduction, clearly demonstrating the control authority of the microflap. The single and dual microflap configurations yield comparable reduction levels of 92% and 93% in the vibration objective, respectively. The dual microflap configuration produces a larger reduction in the vertical shear force and yawing moment compared to the single microflap configuration, but yields a smaller reduction in the longitudinal and lateral shear forces. The five-segment-microflap configuration yields a similar

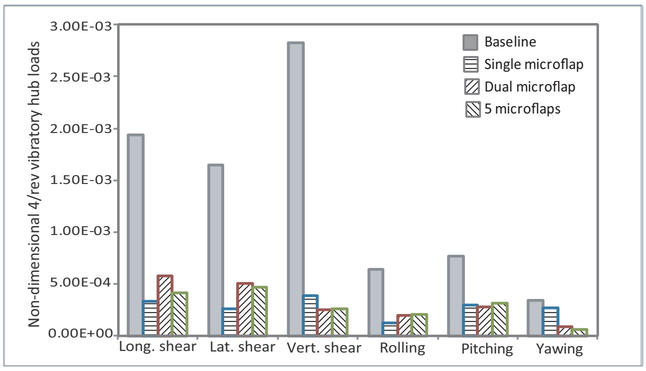

Figure 8. Reduction in 4/rev vibratory hub shears and moments obtained using the single, dual, and 5 microflap configurations.

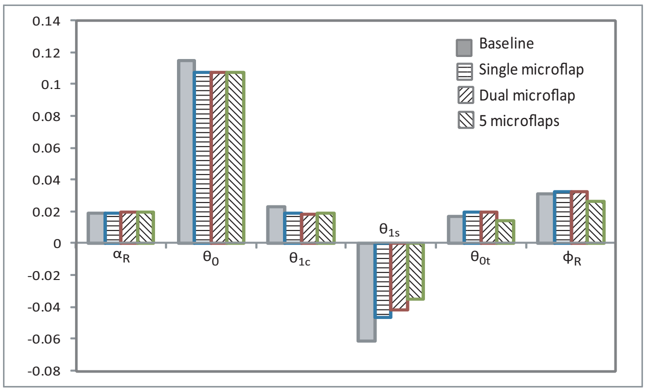

Figure 9. Effect of the various microflap configurations on the rotor trim variables.

performance with a 93% reduction in the overall vibration levels. Note that the vibration objective is a weighted sum of the squares of the 4/rev vibratory hub shears and moments.

As mentioned earlier, the rotor is re-trimmed after engaging the controller. The effect of the microflap deflection on the trim variables during vibration reduction is shown in Figure 9. The cyclic pitch component θ_{1s} is most significantly affected by the microflap deflections, as indicated in Fig. 9. Other trim variables are also somewhat affected with the exception of rotor shaft angle α_R.

The microflap deflection histories for the single and dual microflap configurations over one complete revolution are shown in Figures 10(a) and 10(b), respectively. The saturation algorithm described earlier is used to restrain the microflap deflection between 0%c and 1.5%c which correspond to the retracted and fully deployed positions of the microflap.

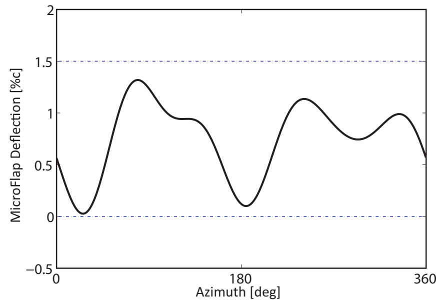

(a) Single Microflap

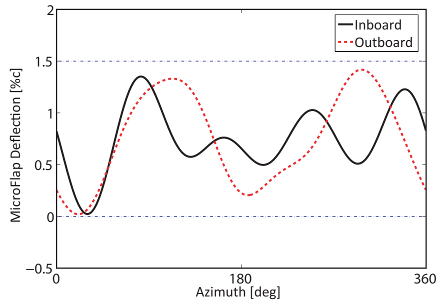

(b) Dual Microflap

Figure 10. Microflap deflection histories over one complete revolution for the single and dual microflap configurations.

Comparison of microflap with plain flap

Next, the capabilities of microflap for vibration reduction are compared to those of the single and dual flap configurations with 20%c trailing-edge plain flaps, under the same BVI flight conditions specified earlier. Vibration levels obtained using the single and dual flap configurations of the conventional plain flap and the microflap are shown in Figure 11. Interestingly, the 1.5%c microflap configurations are more effective in reducing vibration than their plain flap counterparts. The single plain flap configuration yields 83% reduction in the vibration levels, while the single microflap configuration yields almost 9% additional reduction in the vibration levels compared to the single plain flap configuration. Similarly, the dual plain flap configuration yields close to 86% reduction, which is less than the 93% reduction achieved by the dual microflap case.

The plain flap deflection histories for the single and dual flap configurations over one complete revolution are shown in Figures 12(a) and 12(b), respectively. The angular deflection of the plain flap is restricted to $\pm 4°$ as practical saturation limits. The plain flap deflection histories display a notable resemblance to the microflap deflection histories (see Fig. 10), where the peaks and troughs of the deflections occur at approximately same azimuthal loca-

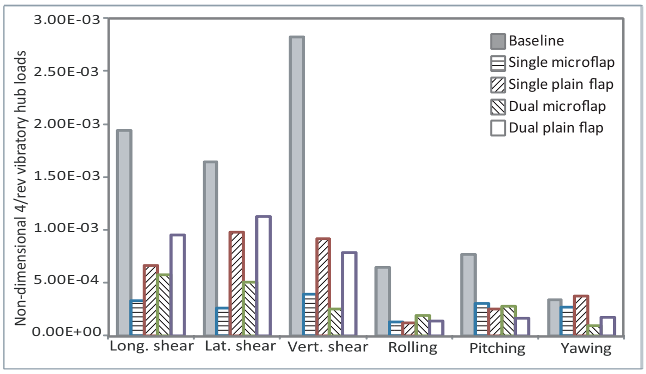

Figure 11. Reduction in 4/rev vibratory hub shears and moments obtained using the single and dual flap configurations of the 20%c trailing-edge plain flap and the 1.5%c microflap.

tions. However, the contributions of higher harmonics (4/rev and 5/rev) are more evident in the case of the plain flaps (Fig. 12).

The significant advantages in vibration reduction demonstrated by microflaps over similarly configured plain flaps are somewhat surprising; therefore, the unsteady effects due to a 20%c plain flap (with $\pm 4°$ deflection) and a 1.5%c microflap on sectional lift and pitching moment are further examined at representative flow conditions encountered by the control surfaces on the rotor blade. A comparison of the oscillatory lift and moment generated by the oscillating plain flap and the microflap is shown in Figures 13(a) and 13(b). These oscillatory loads are obtained for a Mach number $M = 0.45$, airfoil mean angle of attack $\alpha_0 = 2°$, and reduced frequency $k = 0.02$. Both the plain flap and the microflap produce similar peak-to-peak lift amplitudes but the microflap generates a significantly higher maximum lift value. Similarly, the microflap produces a higher maximum nose-down pitching moment on the airfoil than the plain flap. Similar trends have also been observed for other flow conditions. For example, another set of comparisons in the lift and moment generated by the microflap and the plain flap is shown in Figures 14(a) and 14(b) for $M = 0.60$, $\alpha_0 = 2°$, and $k = 0.02$. At this flow condition, the microflap also produces higher maximum lift and maximum nose-down pitching moment than the plain flap, while generating similar peak-to-peak lift and moment amplitudes.

The effect of deploying the various microflap and plain flap configurations for vibration reduction on the rotor power is summarized in Table 2. It is interesting to note that the higher vibration reduction capability of the microflap comes at the cost of increased rotor power penalty. The single microflap configuration yields about 9% higher reduction in

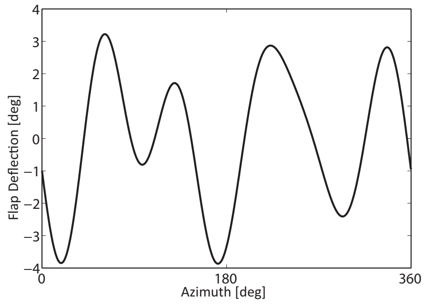

(a) Single plain flap

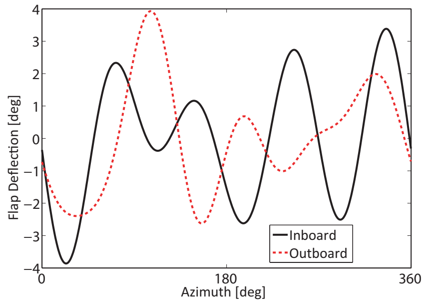

(b) Dual plain flap

Figure 12. Flap deflection histories over one complete revolution for the single and dual plain flap configurations.

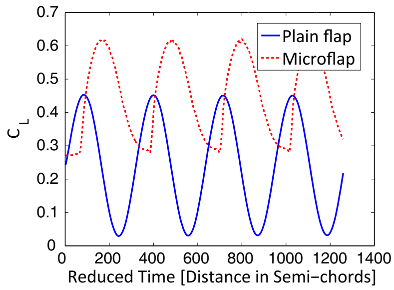

(a) Lift coefficient

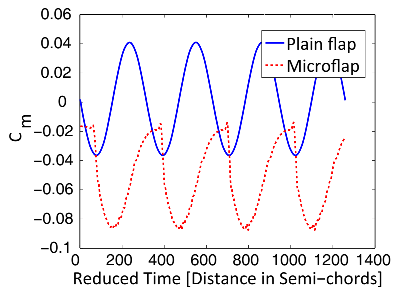

(b) Moment coefficient

Figure 13. Lift and moment coefficient variation on a NACA0012 airfoil due to an oscillating microflap and an oscillating 20%c trailing-edge plain flap. $M = 0.45$, $\alpha_0 = 2°$, **and** $k = 0.02$.

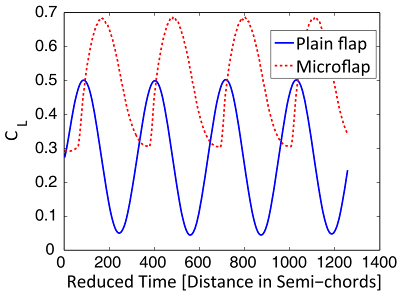

(a) Lift coefficient

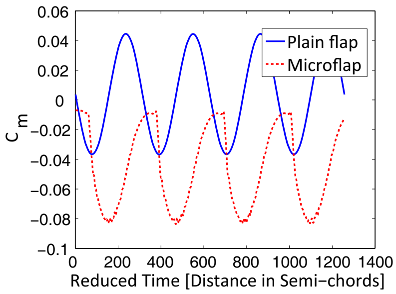

(b) Moment coefficient

Figure 14. Lift and moment coefficient variation on a NACA0012 airfoil due to an oscillating microflap and an oscillating 20%c trailing-edge plain flap. $M = 0.60$, $\alpha_0 = 2°$, **and** $k = 0.02$.

the vibration levels (92% vs 83%); however, vibration reduction with single microflap results in a 3.6% rotor power penalty as compared to 2.4% power reduction using the single plain flap configuration.

To further examine the higher power penalty associated with the microflap, the drag coefficients generated by the oscillating microflap and the oscillating trailing-edge plain flap are compared in Figures 15(a) and 15(b) for Mach numbers 0.45 and 0.60, respectively. It is evident from Figures 15(a) and 15(b) that the drag penalty due to the microflap is significantly higher compared to that due to the plain flap at the same flow conditions. This increase in drag is clearly responsible for the performance penalty as represented by the increased average rotor power. The average rotor power is defined as the instantaneous power required to drive the rotor at a constant angular velocity averaged over one revolution,

$$P_R = \frac{\Omega}{2\pi} \int_0^{2\pi} -M_{Hz}(\psi) d\psi, \tag{13}$$

where M_{Hz} is the total yawing moment about the hub.

Previous studies have found that the lift-to-drag ratio for an airfoil equipped with a Gurney flap is only increased at moderate to high lift coefficients (near stall angles), whereas the L/D ratio is reduced at small angles of attack due to the increased drag [7, 17]. Furthermore, Gurney flap height of greater than 2%c usually results in a significant drag increase [1,15]. The vibration reduction studies conducted here are at a low advance ratio, which corresponds to BVI flight conditions, where the blade operates at relatively low angles of attack in fully attached flow. Consequently, it is not surprising that the microflap used for vibration reduction incurs a significant performance penalty.

Effect of microflap chord size

To investigate further the effect of vibration reduction on rotor performance, vibration reduction studies were conducted using smaller microflaps, with sizes of 0.85%c and 0.50%c. The smaller microflap sizes are implemented by limiting the maximum deflection of the 1.5%c microflap. A comparison of the vibration levels obtained using a 0.5%c microflap, a 0.85%c microflap, a 1.5%c microflap, and a 20%c trailing-edge plain flap with the single flap configuration is shown in Figure 16. The corresponding average rotor power values are listed in Table 3.

Results shown in Table 3 indicate that the 0.85%c microflap yields higher vibration reduction (6% higher) when compared to the plain flap, while simultaneously reducing rotor power by 2.3%, an amount similar to that obtained with the plain flap. The 0.85%c microflap yields slightly less vibration reduction compared to the 1.5%c microflap, while eliminating the performance penalty associated with the larger microflap. An even smaller microflap configuration, the 0.5%c microflap, produces about 7% lesser vibration reduction than the plain flap while demonstrating a remarkable 4.9% power reduction. Since the 0.85%c microflap provides a good compromise between vibration reduction and performance penalty, it may be the most suitable configuration for vibration reduction in rotorcraft. For all three microflap configurations, the deflection histories over one complete rotor revolution are shown in Figure 17. It is evident that the flap deflection time histories for the three microflaps with different sizes are quite similar in overall shape.

Table 2. Effect of vibration reduction using a 1.5%c microflap and a 20%c plain flap on the average rotor power.

	Single		Dual	
	Plain flap	Microflap	Plain flap	Microflap
Baseline power	0.00336516	0.00336516	0.00336516	0.00336516
Power after vib. red.	0.00328327	0.00348505	0.00317784	0.00348640
% change in Power	-2.4	3.6	-5.5	3.6
% Vib. Red.	83	92	86	93

Table 3. Effect of vibration reduction on rotor power using microflaps of various sizes. All results are obtained using single flap configuration.

	1.5%c microflap	0.85%c microflap	0.50%c microflap	20%c plain flap
Baseline power	0.00336516	0.00336516	0.00336516	0.00336516
Power after vib. red.	0.00348505	0.00328610	0.00319791	0.00328327
% change in Power	3.6	-2.3	-4.9	-2.4
% Vib. Red.	92	89	76	83

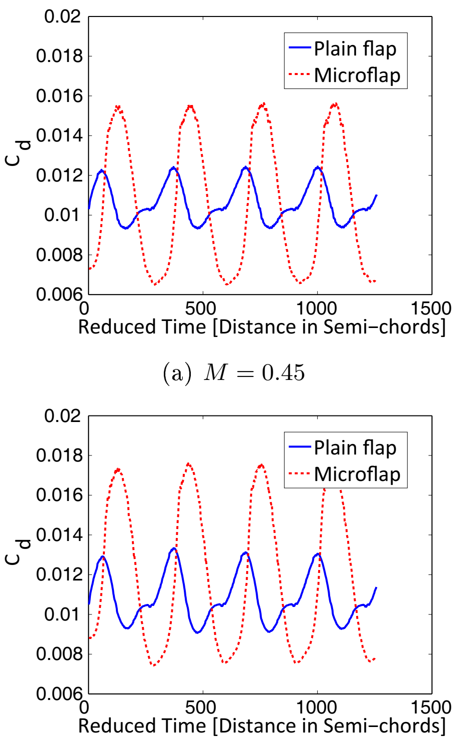

(a) $M = 0.45$

(b) $M = 0.60$

Figure 15. Drag coefficient variation on a NACA0012 airfoil due to an oscillating microflap and an oscillating 20%c trailing-edge plain flap. $M = 0.45$ and 0.60, $\alpha_0 = 2°$, and $k = 0.02$.

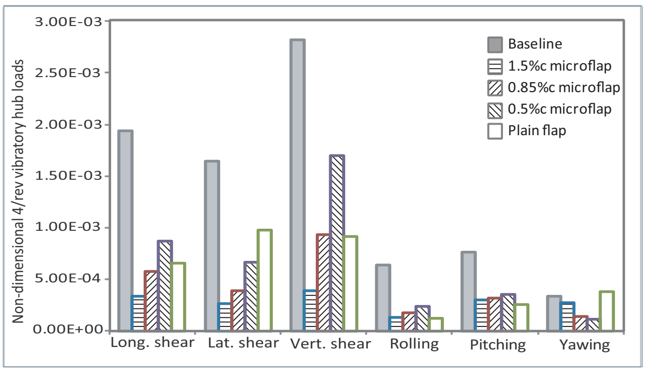

Figure 16. Reduction in 4/rev vibratory hub shears and moments obtained using the single flap configuration with microflaps of various sizes and a 20%c plain flap.

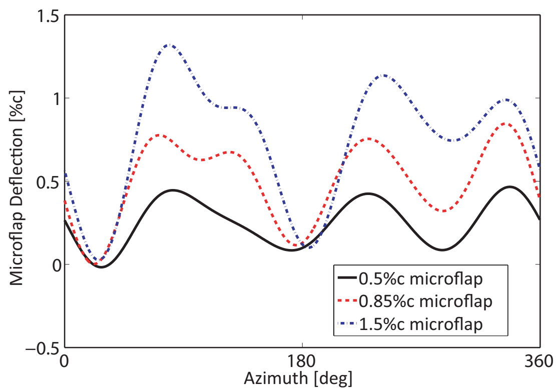

Figure 17. Microflap deflection histories over one complete revolution for microflaps of various sizes.

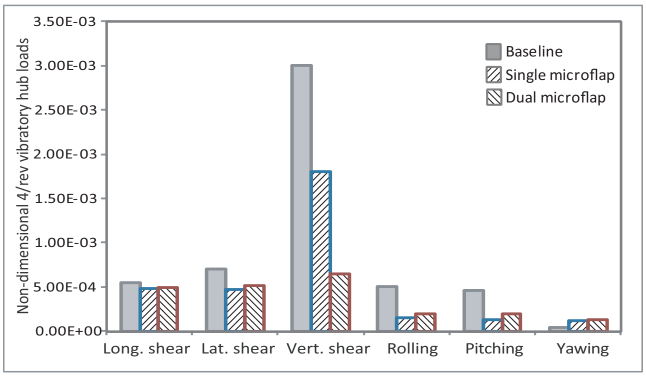

Figure 18. Reduction in 4/rev vibratory hub shears and moments obtained using 0.85%c single and dual microflaps during a $6.5°$ descending flight; $\mu = 0.15$.

Vibration reduction with microflap at different flight conditions

Vibration reduction studies with the single and dual microflap configurations are conducted for descending flight at advance ratio $\mu = 0.15$, descent angle $\theta_{\rm FP} = 6.5°$, and weight coefficient $C_{\rm W} = 0.005$. The descent flight is characterized by high vibratory loads as well as noise due to strong BVI. Vibratory hub loads obtained for the descending flight using 0.85%c single and dual microflaps are shown in Figure 18. The single microflap configuration reduces vibrations by about 71% while the dual microflap configuration yields almost a 87% reduction. The dual microflap configuration produces significantly more reduction in the vertical shear force when compared to the single microflap configuration, while demonstrating comparable reductions for all the other vibration components.

The microflap deflection histories for the single and dual microflap configurations over one complete revolution are shown in Figures 19(a) and 19(b), respectively. As can be seen in the figures, the maximum microflap deflection is restricted to approximately 0.85%c.

The capability of the microflaps for vibration reduction at higher advance ratios of $\mu = 0.20$ and 0.25 is also examined, using the single and dual microflap configurations. These simulations are conducted for steady level flight, and the weight coefficient $C_{\rm W} = 0.005$. The baseline as well as the reduced vibration levels using the 0.85%c microflap configurations are shown in Fig. 20. At the advance ratio of $\mu = 0.20$, The vibration objective is reduced by 89% and 85%, for the single and dual microflap configurations, respectively. The level of vibration reduction that can be obtained at the advance ratio $\mu = 0.25$ is very similar to that obtained at $\mu = 0.20$,

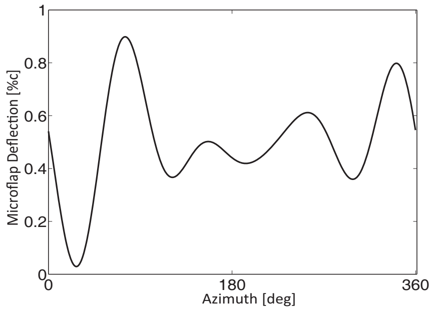

(a) Single Microflap

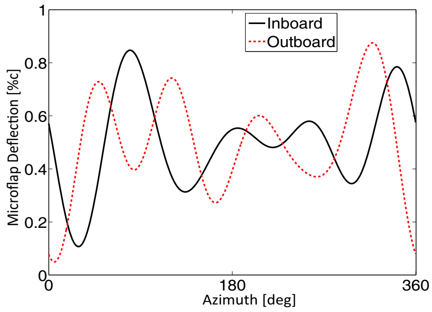

(b) Dual Microflap

Figure 19. Microflap deflection histories over one complete revolution for the 0.85%c single and dual microflap configurations; $\mu = 0.15$ and $\theta_{\rm FP} = 6.5°$.

which is 91% and 85% for the single and dual microflap configurations, respectively. The microflap deflection time histories during the vibration reduction are shown in Fig. 21 and Fig. 22. For the single microflap configuration (see Figs. 21(a) and 22(a)), it is noted that the optimal microflap deflections are similar in overall shape for these two advance ratios. Vibration reduction with the dual microflap configuration at these advance ratios also requires similar microflap inputs, as can be seen from Figs. 21(b) and 22(b). Furthermore, these optimal microflap deflections also bear some resemblance to the $\mu = 0.15$ cases shown earlier in Figs. 17 and 19.

Concluding Remarks

An assessment of the potential of microflap for vibration reduction in rotorcraft is conducted in this paper, using a CFD based ROM combined with the comprehensive rotorcraft simulation code AVINOR. Based on earlier research, a sliding microflap configuration with maximum 1.5%c height was employed. Three spanwise microflap configurations are considered: including a single, a dual, and a segmented five-flap configuration. The single and dual flap configurations are identical to those used in previous studies for conventional trailing edge flaps. The vi-

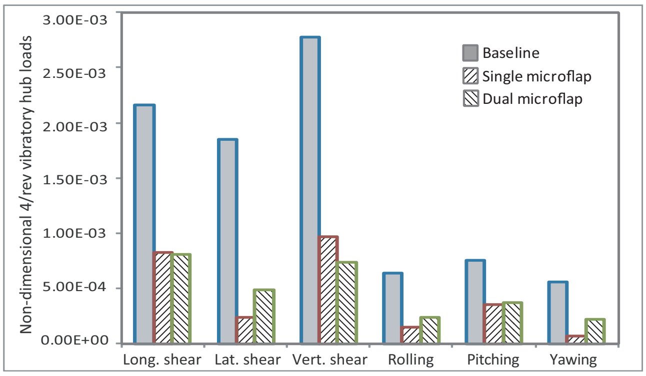

(a) $\mu = 0.20$

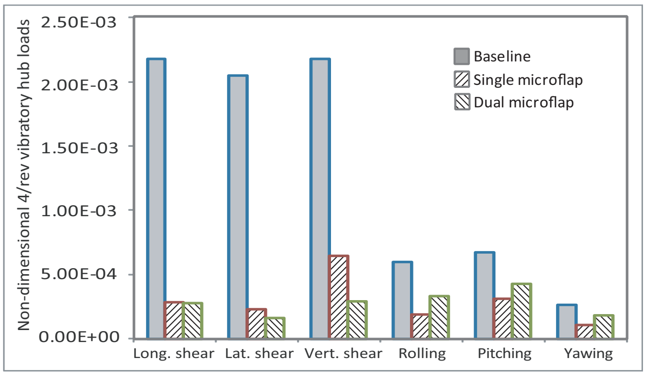

(b) $\mu = 0.25$

Figure 20. Reduction in 4/rev vibratory hub shears and moments obtained using 0.85%c single and dual microflaps during level flight at two advance ratios $\mu = 0.20$ and 0.25.

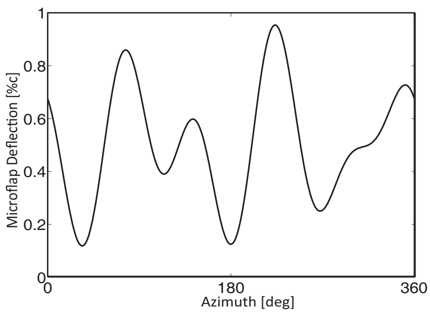

(a) Single Microflap

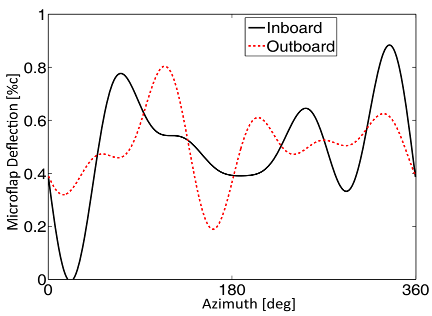

(b) Dual Microflap

Figure 21. Microflap deflection histories over one complete revolution for the 0.85%c single and dual microflap configurations during level flight at $\mu = 0.20$.

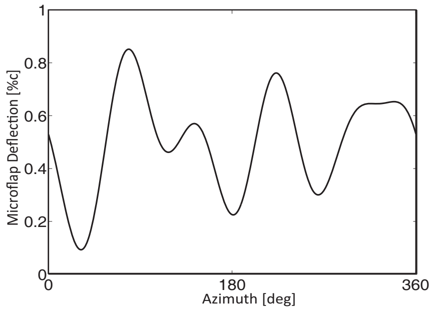

(a) Single Microflap

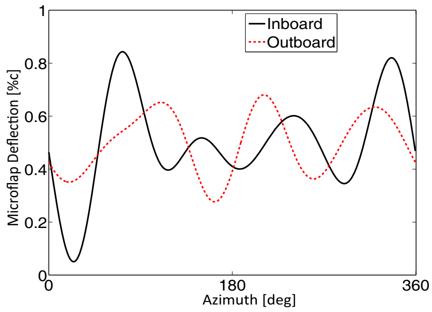

(b) Dual Microflap

Figure 22. Microflap deflection histories over one complete revolution for the 0.85%c single and dual microflap configurations during level flight at $\mu = 0.25$.

bration reduction capabilities for single and dual microflaps are compared to those of 20%c plain flaps. Furthermore, the effect of vibration reduction using microflaps on rotor performance penalty is examined, with parametric studies conducted for various microflap sizes as well as flight conditions. The principal findings of the present study are summarized as follows:

1. The microflap is an effective device for vibration reduction in rotorcraft. A single microflap configuration with chord size of 0.85%c produces 89% vibration reduction under BVI conditions, demonstrating better control authority compared to the 20%c plain flap configuration. A larger microflap (1.5%c) produces more vibration reduction but results in a undesirable performance penalty of 3.6% increase in rotor power.

2. The microflap configuration with flap heights larger than 1%c may incur substantial performance penalty during vibration reduction. For instance, Vibration reduction with the 1.5%c microflap configuration resulted in a 3.6% performance penalty. This is due to the significant drag penalty and the reduced L/D ratio when the microflap is deployed at relatively low airfoil angles of attack. This drag

penalty could be eliminated by using a smaller microflap. It was found that the 0.85%c microflap produces excellent vibration reduction (89%) combined with 2.3% rotor power reduction.

3. All three microflap spanwise configurations considered in this study, including single, dual, and five-segment microflap configurations, have been shown to be capable of reducing vibration levels substantially.

4. The microflaps have been shown to be capable of producing vibration reduction of approximately 90% over a wide range of flight conditions.

Acknowledgments

This research was supported by the Vertical Lift Research Center of Excellence (VLRCOE) sponsored by NRTC and U.S. Army with Dr. M. Rutkowski as grant monitor.

References

[1] Liebeck, R. H. , "Design of Subsonic Airfoils for High Lift," Journal of Aircraft, Vol. 15, (9), Sept 1978, pp. 547–561.

[2] Giguere, P. , Lemay, J. , and Dumas, G. , "Gurney Flap Effects and Scaling for Low-speed Airfoils," Proceedings of the AIAA Applied Aerodynamics Conference, San Diego, June 1995.

[3] Jang, C. S. , Ross, J. C. , and Cummings, R. M. , "Numerical Investigation of an Airfoil With a Gurney Flap," Journal of Aircraft Design, Vol. 1, (2), June 1998, pp. 75–88.

[4] Jeffrey, D. , Zhang, X. , and Hurst, D. W. , "Aerodynamics of Gurney Flaps on a Single-Element High-Lift Wing," Journal of Aircraft, Vol. 32, (2), March-April 2000, pp. 295–301.

[5] Baker, J. P. , Standish, K. J. , and van Dam, C. P. , "Two-Dimensional Wind Tunnel and Computational Investigation of a Microtab Modified S809 Airfoil," Proceedings of the 43rd AIAA Aerospace Sciences Meeting and Exhibit, Reno, NV, Jan 2005. AIAA Paper No. 2005-1186.

[6] Chow, R. and van Dam, C. P. , "Unsteady Computational Investigations of Deploying Load Control Microtabs," Journal of Aircraft, Vol. 43, (5), Sept-Oct 2006, pp. 641–648.

[7] Wang, J. J. , Li, Y. C. , and Choi, K. S. , "Gurney Flap – Lift Enhancement, Mechanisms, and Applications," Progress in Aerospace Sciences, Vol. 44, (1), January 2008, pp. 22–47.

[8] Lee, H.-T. , Kroo, I. M. , and Bieniawski, S. , "Flutter Suppression for High Aspect Ratio Flexible Wings Using Microflaps," Proceedings of the 43rd AIAA/ASME/ASCE/AHS/ACS Structures, Structural Dynamics and Materials Conference, Reno, NV, Apr 2002. AIAA Paper No. 2002-1717.

[9] Kroo, I. M. , "Aerodynamic Concepts for Future Aircraft," Proceedings of the 30th AIAA Fluid Dynamics Conference, Norfolk, VA, Jun-July 1999. AIAA Paper No. 99-2003.

[10] Matalanis, C. G. and Eaton, J. K. , "Wake Vortex Alleviation Using Rapidly Actuated Segmented Gurney Flaps," AIAA Journal, Vol. 45, (8), August 2007, pp. 1874–1884.

[11] Vey, S. , Paschereit, O. C. , Greenblatt, D. , and Meyer, R. , "Flap Vortex Management by Active Gurney Flaps," Proceedings of the 46th AIAA Aerospace Sciences Meeting and Exhibit, Reno, NV, Jan 2008. AIAA Paper No. 2008-286.

[12] Nikolic, V. R. , "Two Aspects of the Use of Full- and Partial-Span Gurney Flaps," Journal of Aircraft, Vol. 44, (5), Sept-Oct 2007, pp. 1745–1748.

[13] Nakafuji, D. T. Y. , van Dam, C. P. , Smith, R. L. , and Collins, S. D. , "Active Load Control for Airfoils using Microtabs," Journal of Solar Energy Engineering, Vol. 123, (4), November 2001, pp. 282–289.

[14] Wilson, D. G. , Berg, D. E. , Lobitz, D. W. , and Zayas, J. R. , "Optimized Active Aerodynamic Blade Control for Load Alleviation on Large Wind Turbines," AWEA WINDPOWER 2008 Conference & Exhibition, Houston, TX, June 1-4 2008.

[15] Kentfield, J. A. C. , "The Potential of Gurney Flaps for Improving the Aerodynamic Performance of Helicopter Rotors," Proceedings of

the AIAA International Powered Lift Conference, 1993. AIAA Paper No. 93-4883.

[16] Maughmer, M. D. , Lesieutre, G. L. , and Kinzel, M. P. , "Miniature Trailing-Edge Effectors for Rotorcraft Performance Enhancement," Proceedings of the 61st Annual American Helicopter Society Forum, Grapevine, TX, June 2005.

[17] Kinzel, M. P. , Maughmer, M. D. , Lesieutre, G. L. , and Duque, E. P. N. , "Numerical Investigation of Miniature Trailing-Edge Effectors on Static and Oscillating Airfoils," Proceedings of the 43rd AIAA Aerospace Sciences Meeting and Exhibit, Reno, NV, Jan 2005. AIAA Paper No. 2005-1039.

[18] Kinzel, M. P. , Maughmer, M. D. , and Lesieutre, G. L. , "Miniature Trailing-Edge Effectors for Rotorcraft Performance Enhancement," Journal of the American Helicopter Society, Vol. 52, (2), April 2007, pp. 146–158.

[19] Friedmann, P. P. and Millott, T. A. , "Vibration Reduction in Rotorcraft Using Active Control: A Comparison of Various Approaches," Journal of Guidance, Control, and Dynamics, Vol. 18, (4), July-August 1995, pp. 664–673.

[20] Friedmann, P. P. , de Terlizzi, M. , and Myrtle, T. F. , "New Developments in Vibration Reduction with Actively Controlled Trailing Edge Flaps," Mathematical and Computer Modelling, Vol. 33, 2001, pp. 1055–1083.

[21] Koratkar, N. A. and Chopra, I. , "Wind Tunnel Testing of a Smart Rotor Model with Trailing Edge Flaps," Journal of the American Helicopter Society, Vol. 47, (4), October 2002, pp. 263–272.

[22] Patt, D. , Liu, L. , and Friedmann, P. P. , "Simultaneous Vibration and Noise Reduction in Rotorcraft Using Aeroelastic Simulation," Journal of the American Helicopter Society, Vol. 51, (2), April 2006, pp. 127–140.

[23] Dieterich, O. , Enenkl, B. , and Roth, D. , "Trailing Edge Flaps for Active Rotor Control Aeroelastic Characteristics of the ADASYS Rotor System," Proceedings of the 62nd American Helicopter Society Annual Forum, Phoenix, AZ, May 2006.

[24] Straub, F. K. , Anand, V. R. , Birchette, T. S. , and Lau, B. H. , "Wind Tunnel Test of the SMART Active Flap Rotor," Proceedings of the 65th Annual AHS Forum, Grapevine, TX, May 2009.

[25] Liu, L. , Padthe, A. K. , and Friedmann, P. P. , "A Computational Study of Microflaps with Application to Vibration Reduction in Helicopter Rotors," Proceedings of the 50th AIAA/ASME/ASCE/AHS/ACS Structures, Structural Dynamics and Materials Conference, Palm Springs, CA, April 2009. AIAA Paper No. 2009-2604.

[26] Padthe, A. K. , Liu, L. , and Friedmann, P. P. , "A CFD-Based Nonlinear Reduced-Order Aerodynamic Model for Comprehensive Simulation of Rotorcraft with Active Microflaps," Proceedings of the 65th American Helicopter Society Annual Forum, Grapevine, TX, May 2009.

[27] Glaz, B. , Friedmann, P. P. , Liu, L. , Kumar, D. , and Cesnik, C. E. S. , "The AVINOR Aeroelastic Simulation Code and Its Application to Reduced Vibration Composite Rotor Blade Design," Proceedings of the 50th AIAA/ASME/ASCE/AHS/ACS Structures, Structural Dynamics and Materials Conference, Palm Springs, CA, May 2009. AIAA Paper No. 2009-2601.

[28] Rogers, K. L. , Airplane Math Modeling Methods for Actively Control Design. AGARD-CP-228, August 1977.

[29] Edwards, J. H. , "Application of Laplace Transform Methods to Airfoil Motion and Stability Calculations," Proceedings of the 20th Structures, Structural Dynamics and Materials Conference, St. Louis, MO, April 1979. AIAA Paper No. 1979-772.

[30] Karpel, M. , Design for Active and Passive Flutter Suppression and Gust Alleviation. NASA Contractor Report 3492, November 1981.

[31] Vepa, R. , Finite State Modeling of Aeroelastic Systems. NASA Contractor Report 2779, 1977.

[32] Myrtle, T. F. and Friedmann, P. P. , "Application of a New Compressible Time Domain Aerodynamic Model to Vibration Reduction in Helicopters Using an Actively Controlled Flap," Journal of the American Helicopter Society, Vol. 46, (1), January 2001, pp. 32–43.

[33] Liu, L. , Friedmann, P. P. , and Padthe, A. K. , "Comparison of Approximate Time Domain Aerodynamics for Flapped Airfoils with CFD Based Results with Applications," Proceedings of the AHS Specialists' Conference on Aeromechanics, San Francisco, CA, January 2008.

[34] Liu, L. , Friedmann, P. P. , and Padthe, A. K. , "An Approximate Unsteady Aerodynamic Model for Flapped Airfoils Including Improved Drag Predictions," Proceedings of the 34th European Rotorcraft Forum, Liverpool, UK, September 2008.

[35] Peroomian, O. , Chakravarthy, S. , Palaniswamy, S. , and Goldberg, U. , "Convergence Acceleration for Unified-Grid Formulation Using Preconditioned Implicit Relaxation," AIAA Paper 98-0116, Reno, NV, January 1998.

[36] Peroomian, O. , Chakravarthy, S. , and Goldberg, U. , "A "Grid-Transparent" Methodology for CFD," AIAA Paper 97-0724, Reno, NV, January 1997.

[37] Allwine, D. A. , Strahler, J. A. , Lawrence, D. A. , Jenkins, J. E. , and Myatt, J. H. , "Nonlinear Modeling of Unsteady Aerodynamics at High Angle of Attack," Proceedings of the AIAA Atmospheric Flight Mechanics Conference and Exhibit, Providence, RI, Aug 2004.

[38] Boor, C. D. , *A Practical Guide to Splines*, Springer-Verlag, 2001.

[39] Kahaner, D. , Moler, C. , and Nash, S. , *Numerical Methods and Software*, Prentice-Hall, 1989.

[40] Press, W. H. , Flannery, B. P. , Teukolsky, S. A. , and Vetterling, W. T. , *Numerical Recipes in FORTRAN 77*, Cambridge University Press, 1992.

[41] Liu, L. , Padthe, A. K. , Friedmann, P. P. , Quon, E. , and Smith, M. J. , "Unsteady Aerodynamics of Flapped Airfoils and Rotors Using CFD and Approximate Methods," Proceedings of the 65th American Helicopter Society Annual Forum, Grapevine, TX, May 2009.

[42] de Terlizzi, M. and Friedmann, P. P. , "Active Control of BVI Induced Vibrations Using a Refined Aerodynamic Model and Experimental Correlation," American Helicopter Society 55th Annual Forum Proceedings, Montreal, Canada, May 25-27 1999, pp. 599–615.

[43] Patt, D. , Liu, L. , Chandrasekar, J. , Bernstein, D. S. , and Friedmann, P. P. , "Higher-Harmonic-Control Algorithm for Helicopter Vibration Reduction Revisited," Journal of Guidance, Control, and Dynamics, Vol. 28, (5), (5), 2005, pp. 918–930.

[44] Cribbs, R. and Friedmann, P. P. , "Actuator Saturation and Its influence on Vibration Reduction by Actively Controlled Flaps," AIAA Paper No. 2001-1467. Proceedings of the 42nd AIAA/ASME/ASCE/AHS/ACS Structures, Structural Dynamics and Materials Conference, Seattle, WA, April 2001.